



Synergism of carbon nanotubes and porous-organic polymers (POPs) in CO₂ fixation: One-pot approach for bottom-up assembly of tunable heterogeneous catalyst



Rana R. Haikal^a, Ahmed B. Soliman^{a,e}, Muhamed Amin^b, Stavros G. Karakalos^c, Youssef S. Hassan^a, Ahmed M. Elmansi^a, Inas H. Hafez^{d,f}, Mohamed R. Berber^{d,g}, Abdou Hassanien^{d,h}, Mohamed H. Alkordi^{a,*}

^a Center for Materials Science, Zewail City of Science and Technology, Sheikh Zayed Dist., 12588 Giza, Egypt

^b Center for Photonics and Smart Materials, Zewail City of Science and Technology, Sheikh Zayed Dist., 12588 Giza, Egypt

^c College of Engineering and Computing, Swearingen Engineering Center, University of South Carolina, Columbia, SC 29208, United States

^d Center for Nanotechnology, Zewail City of Science and Technology, Sheikh Zayed Dist., 12588 Giza, Egypt

^e Permanent address: Chemistry Department, Faculty of Science, Ain-Shams University, Abbassia, Cairo, 11566, Egypt

^f Permanent address: Department of Natural Resources and Agricultural Engineering, Faculty of Agriculture, Damanhour University, 22516, Egypt

^g Permanent address: Department of Chemistry, Faculty of Science, Tanta University, Tanta, 31527, Egypt

^h Current address: J. Stefan Institute, Jamova 39, 1000 Ljubljana, Slovenia

ARTICLE INFO

Article history:

Received 13 September 2016

Received in revised form 12 January 2017

Accepted 3 February 2017

Available online 11 February 2017

Keywords:

Porous-organic polymer
Electrocatalytic CO₂ conversion
Multi-walled carbon nanotubes
Bottom-up assembly
Incipient wetness impregnation of Cu ions

ABSTRACT

A porous-organic polymer (POP) was constructed through bottom-up assembly from its molecular precursors atop multi-walled carbon nanotubes (MWCNTs) in a one-pot synthesis, affording a composite material POP@MWCNTs. The composite was found to be microporous and with pronounced affinity towards gaseous CO₂ (heat of adsorption of ~45 kJ/mol at initial coverage). The composite was characterized through several techniques including gas sorption, FTIR spectroscopy, SEM, AFM, and TEM microscopy, elemental analysis and thermogravimetric (TGA) analyses. The homogenous coating of the POP on top of the MWCNTs was evident from its electron microscopy images. Quantum mechanical calculations for geometry optimization of a fragment of the polymer and of the composite indicated rigidified structure of the POP in contact with the MWCNTs, further supporting and explaining the findings from the gas sorption measurements conducted herein. In addition, the composite was found to be electrochemically active towards CO₂ reduction, surpassing the properties of either of its two components, indicating enhanced interfacial interactions between the MWCNTs and the POP. Moreover, the catalytic behavior of the composite was straightforwardly enhanced through post-synthetic incipient wetness impregnation of Cu(I) ions, demonstrating tunability of the catalyst. This approach delineates a pathway to merge the properties of both families of materials, on the molecular level, aiming to extend the realms of microporous solids into electrocatalytic CO₂ capture and sequestration technologies.

© 2017 Elsevier B.V. All rights reserved.

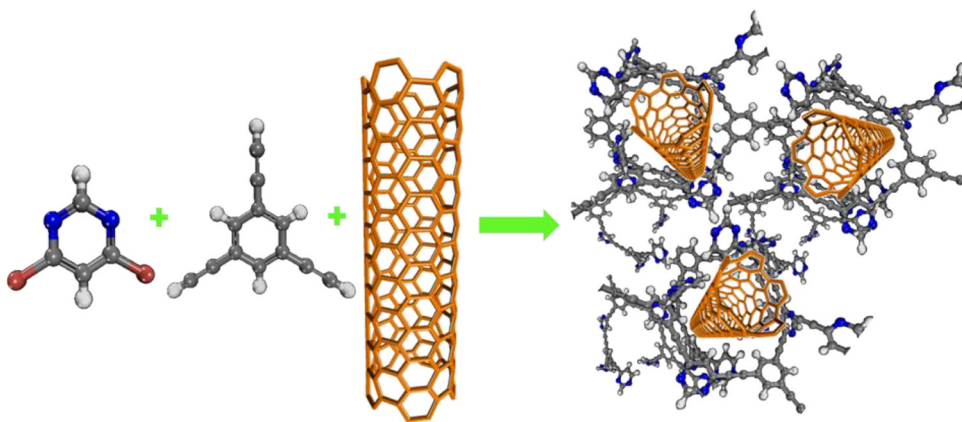
1. Introduction

To alleviate the carbon environmental foot print associated with heavy dependence on fossil fuel, CO₂ capture and sequestration technologies are actively being investigated [1–3]. As novel materials can instigate new technologies, porous solids that can be tailored after specific applications have received considerable

interest in current literature. A large number of such microporous solids are molecular solids, constructed through the bottom-up assembly of molecular building blocks (MBBs), offering a wide range of microporous materials for applications in gas storage and separation, sensing, and heterogeneous catalysis [4–11]. Recent reports outlined several designs of novel solids that can function as heterogeneous catalyst for CO₂ electrocatalytic conversion into feedstock reagents, [12,13] incorporating microporosity and, to some degree, charge mobility. As it is particularly challenging to introduce microporosity, chemical functionality/specifity, and simultaneously maintain good electrical conductivity within the same solid, despite several successful attempts [14–20], we

* Corresponding author.

E-mail addresses: malkordi@mail.usf.edu, [\(M.H. Alkordi\).](mailto:malkordi@zewailcity.edu.eg)



Scheme 1. The one-pot, bottom-up, synthesis of the POP@MWCNTs. C (gray, orange in the CNT), H (white), N (blue), Br (break red). (For interpretation of the references to colour in this figure legend, the reader is referred to the web version of this article.)

opted to explore compounding two largely distinct solids, a porous-organic polymer and carbon nanotubes, through one-pot synthesis. Examples of conductive porous materials include the works of Dinca and co-workers who deposited an intrinsically conductive, and catalytically-active, metal-organic framework (MOF) on electrode surface for application in oxygen reduction reaction [21], used conductive MOFs for chemical sensing [22], and also reported on altering the electrical properties of covalent-organic frameworks (COFs) through diffusing chalcogenides guests [23]. Lu et al. have circumvented the poor electrical conductivity and chemical stability of a certain MOF by utilizing the MOF as a template to grow 3D porous and conductive polyaniline network [24]. COF immobilization on chemically-modified graphene was also recently reported to construct supercapacitor electrodes [25]. Bien and co-workers have demonstrated the ability to

construct the first photovoltaic device from COFs utilizing specific building blocks as photoactive donor-acceptor junction [26]. In a recent report, Xu et al. demonstrated the ability to deposit mesoporous COF on CNTs targeting Li-ion battery applications [27]. Among the widely investigated materials for CO₂ capture, storage, and sequestration are porous organic polymers (POPs) [28–33]. Another fascinating family of materials with excellent mechanical, thermal and electrical properties is the carbon nanotubes (CNTs) [34,35]. Both types of materials exhibit unique properties that are intimately linked to their chemical composition and forms. The wide contrast in their synthesis conditions imposes limitations on constructing composite materials of both in attempt to benefit from their mutual properties, including unsurpassed structural rigidity, electrical and thermal conductivity of CNTs [36,37], chemical functionality and tunable microporosity of POPs. POPs are constructed through *bottom-up* assembly of suitable soluble precursors under several reaction pathways. Among which, the Sonogashira-Hagihara (SH) cross coupling reactions resulted in a relatively large number of such materials utilizing designed molecular building blocks (MBBs) [9,38]. In general, POPs constructed through SH reactions demonstrated highly cross-linked networks maintaining the chemical functionalities of the precursor MBBs. It is due to the wide range of available MBBs that detailed composition-property relationships can be attained, which are essential to enhance the understanding of gas-solid interactions at the molecular level [31]. However, the irreversible nature of covalent linkage employed in constructing the above-mentioned POPs resulted largely in amorphous solids with uncontrollable chain/grain sizes and insoluble materials that are amenable to chemical modification [39], but difficult to process, post-synthetically, into desirable forms like membranes, filters, and thin films needed for certain applications.

In this report, we explored the potential of constructing a POP of appreciable affinity towards CO₂ atop multi-walled CNTs (MWCNTs), in attempt to construct a composite material for CO₂ catalytic conversion. As recently reported by us, the pyrimidine-based POP can feasibly be coated on graphene with no prior chemical modification, and thus we attempted in this study the one-pot construction of this specific POP on MWCNTs [40]. This approach does not require modifying the surface functionality of the MWCNTs prior to compositing with the POP, and hence is of interest. In the presented one-pot approach, the POP was constructed from its soluble molecular precursors in presence of the pristine MWCNTs, and to the best of our knowledge this approach was not previously explored for POPs-MWCNTs composite targeting applications in CO₂ capture and sequestration.

2. Results and discussion

In attempt to seek a plausible approach to augment the structural rigidity, conductivity, and processability of POPs, pristine MWCNTs were utilized as additive, dispersed into the one-pot reaction mixture containing the MBBs necessary to construct a targeted POP, **Scheme 1**. The POP explored here was constructed through SH cross-coupling of the ditopic bromopyrimidine and tritopic terminal alkyne, in presence of MWCNTs dispersed into the synthesis mixture through brief sonication, resulting in composite material of MWCNTs coated homogenously with the POP, referred to here as POP@MWCNTs. Fourier-transform infrared spectroscopy (FT-IR) was utilized to confirm the presence of the POP in the composite, as shown in **Fig. 1**. The FT-IR spectrum for the POP@MWCNTs showed several peaks characteristic of the POP, including the internal $\nu_{C=C}$ stretching at 2215 cm⁻¹, pyrimidine $\nu_{C=N}$ stretching at 1564 cm⁻¹ and absence of the terminal ν_{C-H} stretching expected at ~ 3200 cm⁻¹ for the starting triethynylbenzene. Further characterization for the composition of the resulted composite was accomplished through elemental analysis, indicating significant changes to C and N contents for the POP@MWCNTs as compared to the POP. The observed trend of increased C content and decreased N content, when comparing the POP to the POP@MWCNTs, is expected due to incorporation of purely carbon-based MWCNTs into the matrix of the POP. The elemental analysis results, shown in the supporting information (SI), indicated the following composition for the POP (POP@MWCNT): C, 71.53% (79.65%); H, 2.66% (2.28%); N, 21.14% (7.88%). Additional characterization of the POP and the POP@MWCNTs was conducted through thermogravimetric analysis (TGA, SI). The TGA analyses revealed thermal stability of the POP up to ~ 350 °C, after which a noticeable and gradual weight

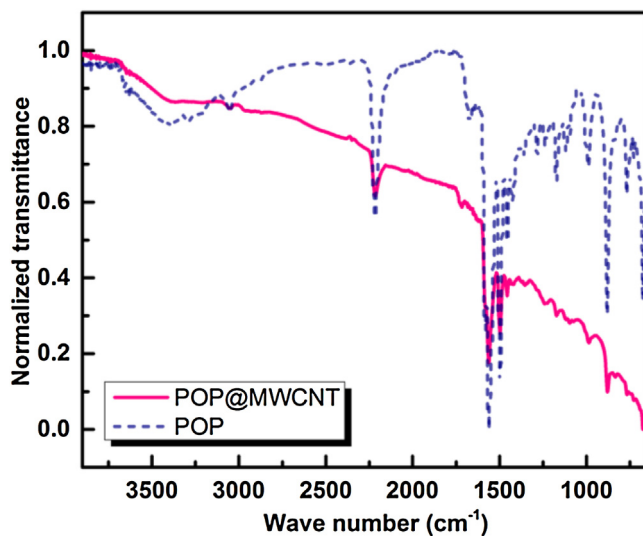


Fig. 1. FT-IR spectra for the POP (dashed line) and the POP@MWCNTs (solid line).

loss was observed due to thermal degradation of the polymer, and the same behavior was also observed for the composite. Interestingly, a noticeable weight loss ~ 5 wt% was observed for the POP below 100°C and can be ascribed to loss of moisture and gaseous species adsorbed inside the pores of the POP.

Due to abundance of basic binding sites (N atoms in the aromatic pyrimidine rings) in the POP, it was shown previously [31] to demonstrate favorable binding energy towards CO₂, and thus presented a suitable target for this investigation. Both the pristine POP and the POP@MWCNTs were found to be porous with comparable apparent surface area, as calculated using Brauner-Emmet-Teller (BET) model, Fig. 2 (BET surface area of 664 m²/g and 452 m²/g, respectively). The surface area for the MWCNTs was also measured (BET surface area of 78.8 m²/g, Fig. 2), confirming that the porosity of the composite is mostly attributed to the POP rather than the MWCNTs.

Applying the non-local density function theory (NLDFT) model of carbon finite pores to the adsorption points in the three samples permitted calculations of the corresponding pore size distribution (PSD), Fig. 2. The PSD histograms demonstrated close resemblance between the POP and the POP@MWCNTs samples, which is in further agreement with the BET surface area findings discussed

above. The pristine POP demonstrated noticeable volume shrinkage upon desolvation prior to gas sorption measurements and H2-type hysteresis towards N₂ sorption. This hysteresis can be ascribed to somewhat structural flexibility and breathing of the material upon N₂ uptake, or alternatively can be ascribed to interparticle condensation [38,41]. Interestingly, the POP@MWCNTs composite did not demonstrate such volume shrinkage upon desolvation nor the sorption hysteresis behavior, indicating rigidified structure, yet with maintained microporosity. The isosteric heat of adsorption (Q_{st}) towards CO₂ into the POP and POP@MWCNTs were also measured through variable temperature CO₂ sorption isotherms, Fig. 3. Both showed nearly identical Q_{st} for CO₂ adsorption (~ 42 –45 kJ/mol at initial loadings), further confirming that adsorption in the composite is taking place largely within the pores of the POP. From the above, it is reasonable to ascribe the observed structural augmentation while maintaining similar behavior towards N₂ sorption within the composite to synergy between the two components brought into contact at the molecular level.

To further investigate the origin of the pronounced structural rigidity of the POP once composed with the MWCNTs, geometry optimization calculations were conducted for the POP and for the POP@CNT using the B3LYP hybrid functional, please see experimental section for details. Due to computational limitations, we opted to utilize a single-walled CNT in our model, which was assumed to represent the nature of surface interactions between the POP and the MWCNT in the composite studied here. The geometry optimized oligomer of the pristine POP is shown in Fig. 4 and indicated presence of intramolecular hydrogen bond interactions between pyrimidine rings, D(C–H..N) = 3.185, 3.266, 3.293, 3.382 Å, and corresponding bond angles θ (C–H..N) = 147.0, 100.6, 169.6, 137.1°, respectively. Such hydrogen bond interactions appear to contribute towards the tortuousness of the POP backbone and thus can potentially contribute to the breathing or structural flexibility of the POP, as indicated by the hysteresis of its N₂ sorption isotherm. The geometry optimized structure of the POP@CNT, Fig. 4, indicated detectable changes to the POP backbone due to interactions with the surface of the CNT. Such changes included weakened intramolecular hydrogen bond interactions between pyrimidine rings in the composite, D (C–H..N) = 3.194, 3.279, 3.444 Å, and the corresponding bond angles θ (C–H..N) = 144.6, 159.6, 133°, respectively. Additionally, the backbone of the POP in the composite was found to undergo noticeable bending around the curved surface of the CNT as judged by shortened end-to-end distances of

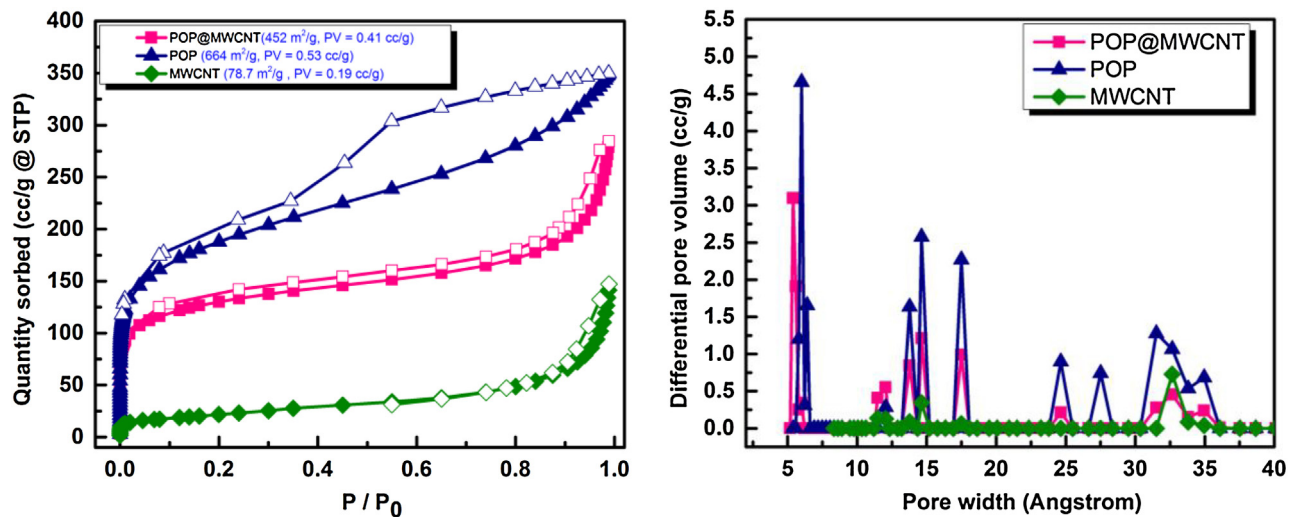


Fig. 2. (left) N₂ sorption isotherms for the MWCNTs, POP, POP@MWCNT, and (right) the corresponding PSD.

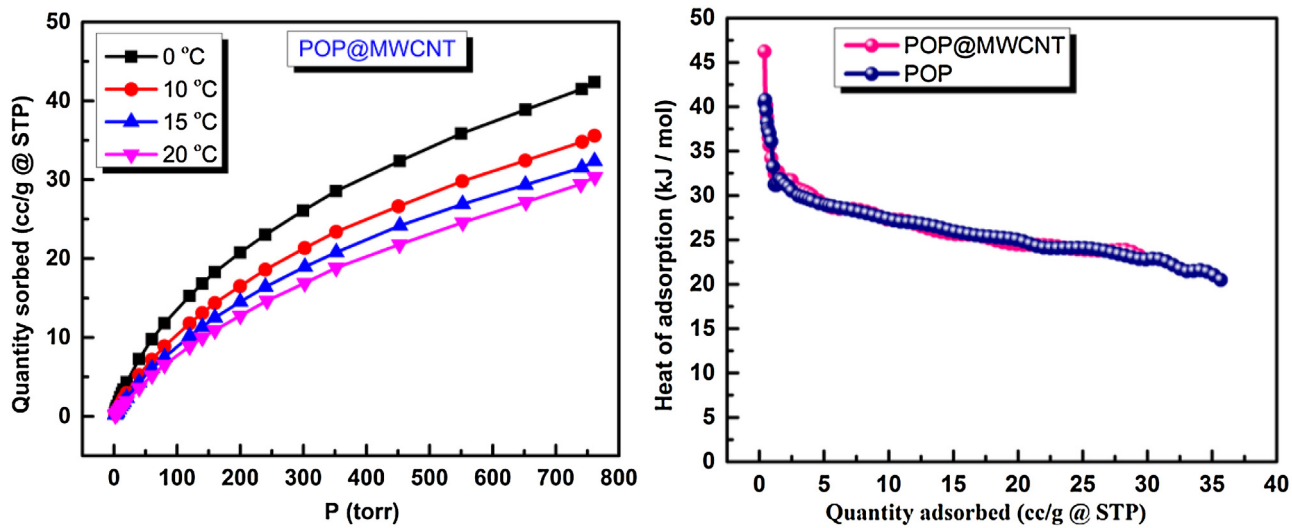


Fig. 3. CO₂ sorption isotherms for the POP@MWCNTs, and the corresponding Q_{st} plot, labeled graphs.

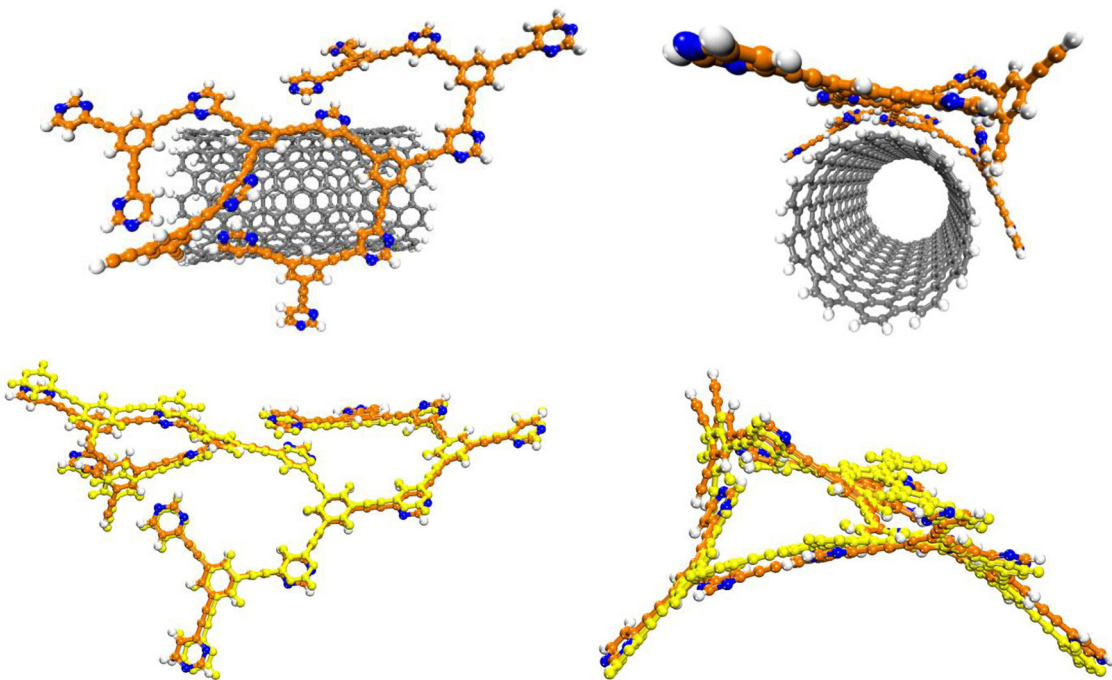


Fig. 4. (top) Two different orientations of the B3LYP 3–21G geometry optimized structure of the POP in contact with the CNT and (below) superimposed geometrically optimized structures for the POP before and after introducing the CNT (geometry changes due to interactions with the CNT are highlighted in yellow). C (orange for the POP and gray for the CNT), N (blue), H (white). (For interpretation of the references to colour in this figure legend, the reader is referred to the web version of this article.)

the POP fragment, see Fig. 4 for the two structures. Therefore, it is reasonable to ascribe the observed fully reversible N₂ sorption isotherm recorded for the composite to have emerged from rigidified backbone of the POP once in contact with the surface of the MWCNTs.

Scanning electron microscopy (SEM) was then utilized to characterize the POP@MWCNTs, Fig. 5, and showed intimate entanglement of the two chemically-distinct species. The SEM images showed no clustering or segregated agglomeration of the POP particles, but rather uniform coverage on the MWCNTs. The uniform coverage of the POP on the MWCNTs was further confirmed through atomic force microscopy (AFM) and transmission electron microscopy (TEM). The AFM image, Fig. 6, demonstrated a rope of POP@MWCNTs, the insert showing more detailed measurement of the POP@MWCNTs, again demonstrating a uniform coating of the

MWCNTs by the POP. Further proof of the uniform coating of the MWCNTs by the POP is shown in the TEM images for a sample of the composite, Fig. 7, and demonstrated a relatively thick layer of the POP wrapping each of the MWCNTs.

The thickness of the POP layer was estimated to be about 15–20 nm with uniform coverage over the whole surface of the MWCNTs. This was further supported by our inability to obtain atomically-resolved images for any of the MWCNTs due to homogeneous coverage by the amorphous polymer, rendering each MWCNT deeply buried inside a thick wrap of the porous POP matrix. The amorphous and porous texture of the POP is also visible in the high magnification TEM image, Fig. 7.

As the POP utilized in this study is shown to be of good affinity towards CO₂, we opted to investigate the potential of POP@MWCNTs towards CO₂ electrocatalytic reduction. The pris-

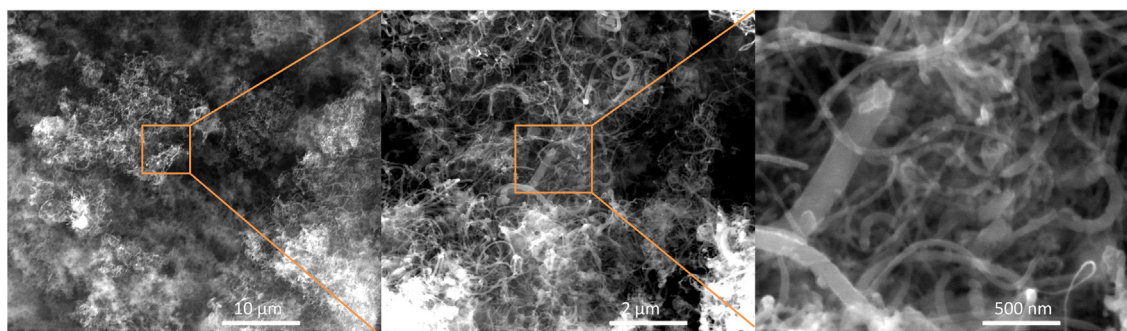


Fig. 5. SEM images of POP@MWCNT at different magnifications (6000/25,000/100,000 X) showing uniform coverage of the POP atop the MWCNTs.

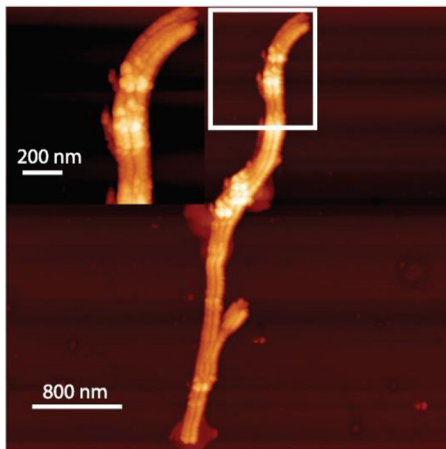


Fig. 6. Tapping mode AFM topographic image showing a rope of MWCNTs covered with the POP. The insert is a close up image taken for the part near the edge of the rope.

tine POP was tested and found to be largely insulating under the conditions utilized below, in contrast to the composite POP@MWCNTs which behaved well in the electrochemical study conducted herein. To investigate the catalytic activity of the composite, a measurement setup was selected as reported earlier to be suitable for CO_2 electrocatalytic reduction in KHCO_3 solution, saturated with CO_2 at 1 atm. [42]. In our setup, we utilized the carbon paste electrode (CPE) method to construct our working electrodes. The reduction current recorded for the CPE, taken as a control, demonstrated a monotonic increase of current vs. potential beyond an onset potential of -1.49 V (SI). Modifying the CPE with 25 wt% POP@MWCNTs resulted in a different trend in the current versus potential curve. A cathodic peak was observed with an onset potential around -0.4 V , followed by a second cathodic wave with an onset potential at -1.22 V . We assigned the first cathodic peak to the reduction of trapped oxygen inside the POP pores, while

the latter was ascribed to the CO_2 electroreduction in parallel with hydrogen evolution reaction [42]. This assignment was further supported by the observed intensity gain of the first cathodic peak when the solution was bubbled with O_2 (SI). Furthermore, within this steady state conditions of a stationary electrode, where convection is kept minimal and gas diffusion is assumed dominant, the oxygen reduction wave was found to fade with time (complete attenuation after few cycles, Fig. 8a). This observed behavior can be explained assuming relatively slow diffusion of CO_2 into the electrode, substituting trapped oxygen inside the pores of the POP. Therefore, it is reasonable to assume that the first reduction wave, recorded at onset potential of -0.4 V , and more prominent in the few earliest recorded voltammograms, to have originated from oxygen reduction. The source of this polymer-trapped oxygen is most likely the atmospheric oxygen adsorbed inside the pores of the POP. This assumption is further supported by the EDX analysis of the composite, which indicated appreciable presence of oxygen into the material even under the vacuum condition inside the chamber of the SEM (SI). From the above, it is concluded that the POP@MWCNT acted as a catalyst in catalyzing CO_2 reduction, with enhanced reduction current onset for the composite as compared to the CPE.

The porous nature of the POP and the decoration of the pores by pyrimidine rings encouraged us to attempt post synthetic modification of the electrode through incipient wetness impregnation method in a solution of CuBr in acetonitrile as a source of Cu ions. Indeed, and most straightforwardly, simple incubation of the POP@MWCNTs in 10 mM acetonitrile solution of CuBr at room temperature for 24 h resulted in uptake of the Cu ions by the composite as indicated from UV-vis spectroscopic measurements of the impregnation solution (SI). The Cu ions impregnation affected the electrochemical catalytic behavior of the composite favorably, Fig. 8b. A detectable enhancement of the electrode's catalytic activity was noticed (earlier observed catalytic wave, and $\sim 75\%$ enhancement in current density at -1.5 V for the POP-Cu@MWCNTs as compared to the POP@MWCNTs (-1.6 mA/cm^2 to -2.8 mA/cm^2 , respectively). To decipher the potential contribution

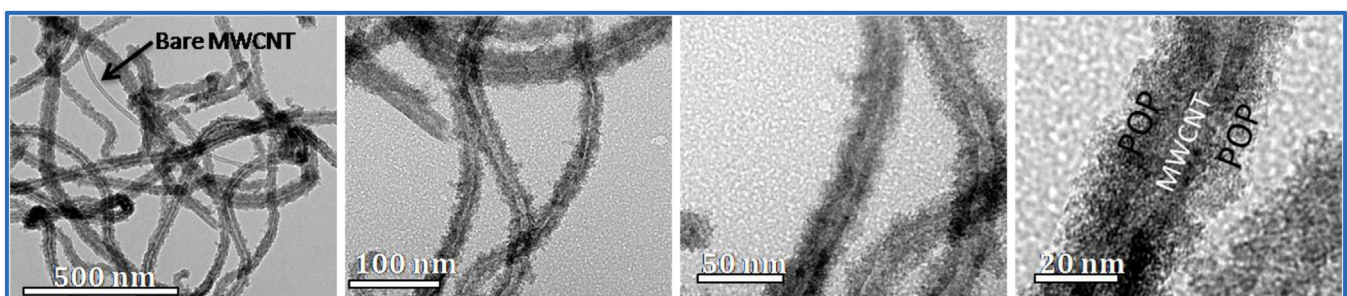


Fig. 7. Different magnifications TEM images of the POP@MWCNTs, showing uniform wrapping of the MWCNTs by the POP.

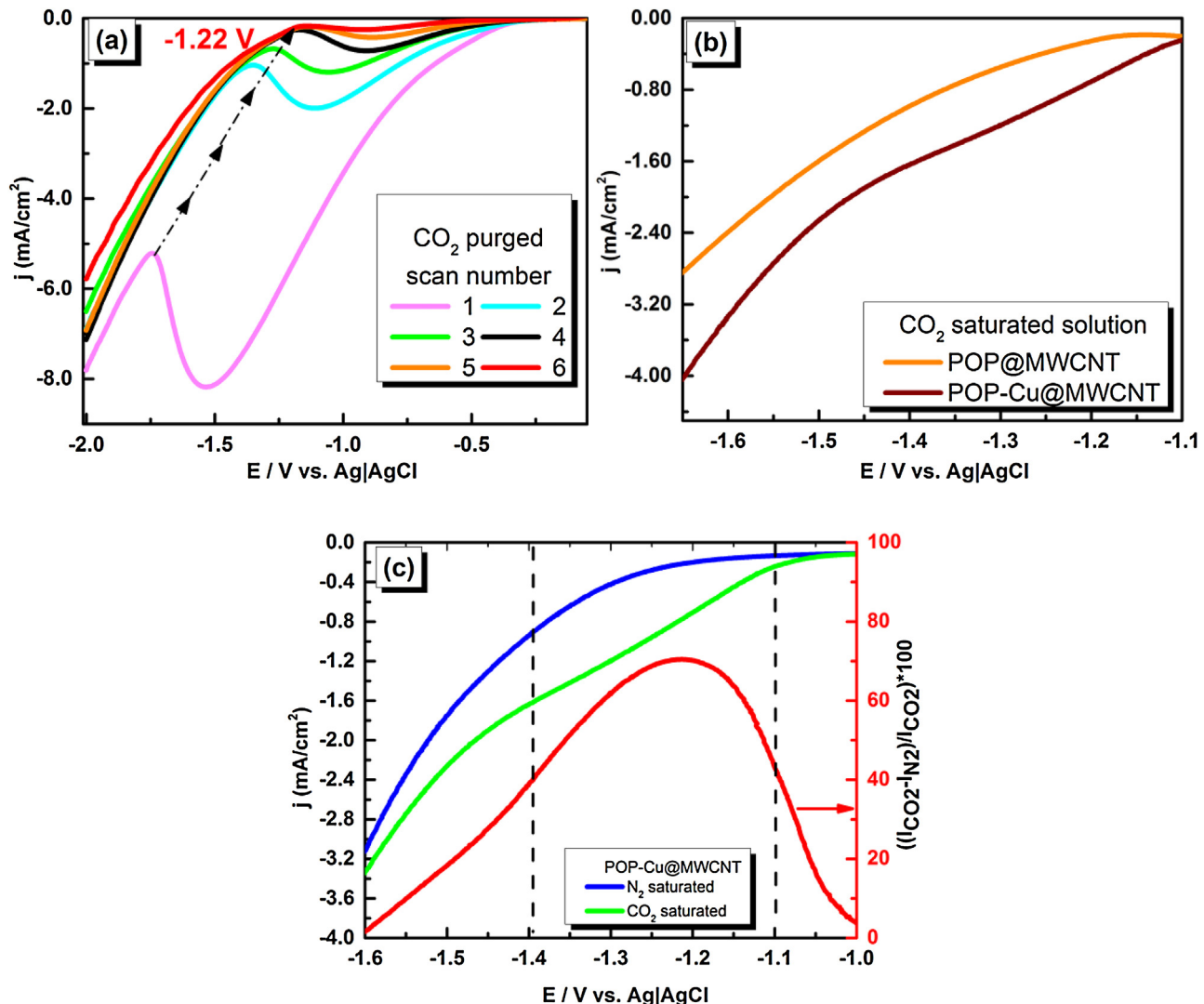


Fig. 8. (a) Electrochemical reduction of CO_2 using the POP@MWCNT-CPE showing successive cycles after insertion into the solution, (b) the electrode behavior after incipient wetness impregnation of Cu ions, and (c) the different electrochemical responses of POP-Cu@MWCNT in N_2 and CO_2 saturated solutions with insert showing CO_2 contribution to the collected current, all measurements were conducted in 0.1 M KHCO_3 aqueous solution, scan rate of 10 mV/s.

of proton reduction activity from CO_2 reduction, two LSVs were collected in N_2 -saturated solution and in CO_2 -saturated solution, Fig. 8c. The two LSVs clearly demonstrated that CO_2 reduction is observed in our material besides concomitant and unavoidable proton reduction. However, a significant contribution to the collected current can be attributed to CO_2 reduction, as evident from the difference between the two current densities collected in the CO_2 -saturated and the N_2 -saturated (pre-degassed) solution, Fig. 8c. In addition, the percentage of current associated to CO_2 reduction, red trace in Fig. 8c, was calculated from difference between the two LSVs, and demonstrated a maximum ($\sim 70\%$) at a potential of -1.22 V, the onset potential for CO_2 reduction. The two dashed lines in Fig. 8c are guides indicating two distinct regions of the LSV collected in the CO_2 -saturated solution, where a steeper slope is evident in between the potential window of -1.1 to -1.4 V, as compared to the potential window more cathodic than -1.4 V. This observation is in agreement with proposed two concomitant electroreduction processes, CO_2 and proton reduction, with the later more pronounced at more cathodic potential. In order to further characterize the electrode material, several cyclic voltammetry measurements (CVs) were collected for the POP-Cu@MWCNTs where the potential of the working electrode was swept from -1

to $+1$ V vs. $\text{Ag}|\text{AgCl}$ with a scan rate of 0.1 V/s, in N_2 and CO_2 saturated 0.1 M KHCO_3 solutions (pH of 8.9 and 6.8 , respectively). The CV measurements conducted on the POP-Cu@MWCNTs modified electrode clearly demonstrated Cu redox process(s) noticed previously in similar systems [43]. In our measurements, we observed clear differences in the CV responses for the electrode material depending on if the CV measurement was conducted before or after running the LSV experiment, Fig. 9. When the CV measurement was conducted before running the LSV, a significant cathodic wave was observed at -0.1 V, close to the onset potential expected for Cu reduction. This is in contrast to the CV conducted on an electrode used previously in an LSV measurement, where the CV in this case demonstrated a small plateau ascribed to Cu reduction process. Our explanation for this observation is that the electrode material, as prepared through Cu(I) ion impregnation, mostly contained the Cu in its ionic form, which then undergo reduction upon sweeping the electrode potential to a negative potential, and thus the reduction wave is most prominent in the CV that was run before conducting the LSV experiment. In Fig. 10a, the first and second CVs measured in the N_2 saturated solution showed noticeable differences, where in the first CV three anodic peaks were observed (highlighted by the three vertical dashed lines) at -0.3 , -0.06 V,

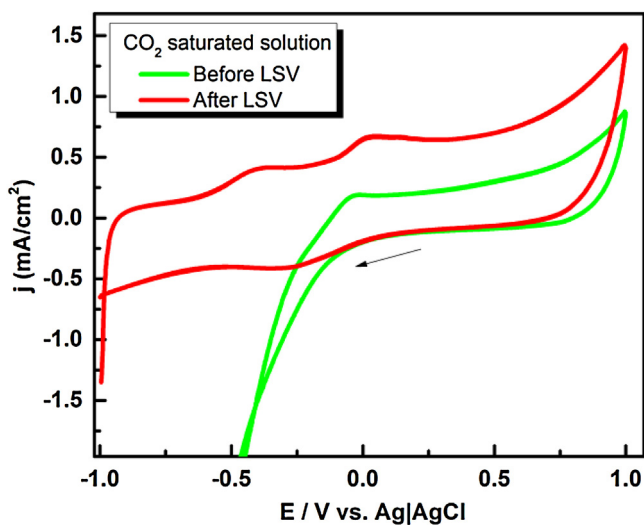


Fig. 9. Cyclic voltammograms for the POP-Cu@MWCNTs-CPE before (green trace) and after (red trace) running the LSV scan in the CO_2 saturated 0.1 M KHCO_3 aqueous solution. (For interpretation of the references to colour in this figure legend, the reader is referred to the web version of this article.)

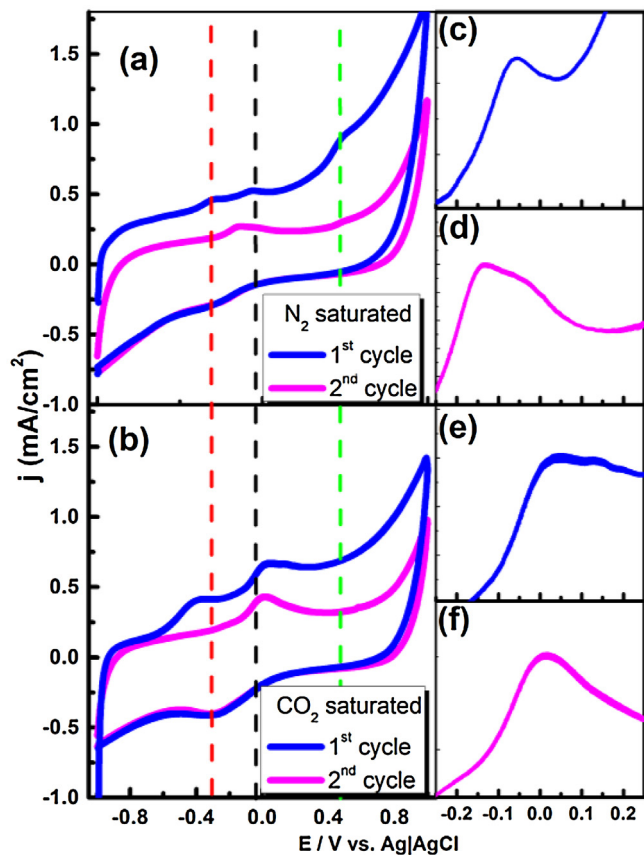


Fig. 10. CV diagrams for the POP-Cu@MWCNT modified electrode in (a) N_2 and (b) CO_2 saturated 0.1 M KHCO_3 aqueous solutions, inserts c-f show magnified parts of the CVs in the left panel for the oxidation peaks at $-0.15 \sim +0.15$ V.

and $+0.45$ V, whereas only one, relatively wide, anodic peak at -0.14 to -0.01 V was observed in the second run. It is worth mentioning that the CV measurements were conducted on an electrode utilized previously for the LSV measurement, and thus the potential was scanned to more negative potential prior to recording the CV voltammograms. Consulting the literature for similar systems of

Cu/HCO_3^- , it appeared that the first anodic peak can be ascribed to adsorbed hydrogen, generated through the previous LSV cathodic scan, the second peak to Cu oxidation (formation of Cu_2O , CuO , and/or Cu carbonates), while the third peak/plateau can be assigned to a passivation process in the basic carbonate solution [44].

The cathodic scan showed only one peak at -0.3 V and was assigned to reduction of the Cu carbonate/hydroxide species [44,45]. In support to this assignment, the second CV demonstrated only the Cu oxidation peak and the corresponding reduction peak. The absence of the adsorbed hydrogen peak in the second CV can be justified based on the potential window we utilized in our CV measurements, where the potential was not scanned beyond or near the hydrogen reduction wave when the first CV was measured. Inserts (c-f) in Fig. 10 are magnified parts of the CVs showing the Cu oxidation peaks within the potential window of ± 0.15 V. As previously reported [44,45], the Cu_2O and CuO formation peaks in similar systems are closely spaced and it appeared that in our case the two peaks coalesced together, most probably due to the chemical nature of our pyrimidine-rich matrix. In fact, the peaks presented in inserts (c) and (d) are broad enough (~ 200 mV) to mask the closely spaced $\text{Cu}_2\text{O}/\text{CuO}$ peaks observed in other systems [44,45], and we were not successful in resolving those peaks even if slower scan rate was applied (data not shown). Alternatively, this broad anodic peak/plateau can be ascribed to formation of Cu carbonate(s) on Cu_2O , where more in-depth investigations are required to unequivocally determine the nature of the formed specie. The assumption of formation of Cu carbonate(s) is further supported by the enhanced peak intensity when the CV was measured in CO_2 saturated solution, Fig. 10b. The first CV that was run immediately after an LSV experiment demonstrated the adsorbed hydrogen peak at -0.4 V and a Cu oxidation peak at $+0.04$ V. In this CV, no noticeable passivation peak was observed, which can be ascribed to the more acidic pH of this solution as compared to the N_2 saturated one. It is obvious from comparing peak positions for the Cu oxidation in inserts (c) and (e) that a shift towards less negative potential was observed in case of the CO_2 saturated solution, suggesting stabilization of the formed oxide. Indeed, it is known that carbonate has good binding affinity towards Cu_2O surface, and it is assumed that this is the case observed here in the CO_2 saturated solution. The second CV scan showed similar trend to that recorded in the second CV scan for the N_2 saturated solution, albeit with noticeable shift of the Cu oxidation peaks to less negative potential, see peaks in inserts (d) and (f).

In order to obtain detailed information about the Cu loading in the sample, X-ray photoelectron spectroscopy (XPS) was conducted on the CuBr exchanged sample. The survey spectrum (SI) indicated near surface composition (wt%) of C (80.8), N (9.2), O (5.3), Br (3.9), and Cu (0.8). The detailed element spectra are shown in Fig. 11 (labelled spectra). In the $\text{Cu} 2p_{3/2}$ spectrum, two components were detected and can be ascribed to Cu(I) (recorded at 932.2 eV and attributed to CuBr and/or Cu_2O) and Cu(II) (detected at 934.7 eV and assigned to $\text{Cu}(\text{OH})_2$) [46,47] with accompanying satellite peaks appearing at higher binding energies. The Br 3d spectrum was deconvoluted into two components (68 eV assigned for C-Br as termination sites for the POP) [48] and (70.2 eV assigned for Cu(I)-bound bromide) [47,49]. The C 1s spectrum was deconvoluted into several components, in agreement with previous values observed for similar systems incorporating MWCNTs [50]. The N 1s spectrum was deconvoluted into two components (398.8 eV assigned to the pyrimidine rings of the POP) and (400.2 eV assigned to the N atoms coordinated to Cu species). The O 1s spectrum was deconvoluted into three components, (530.7 eV, attributed to Cu_2O) [47,51], (531.9 eV attributed to isolated OH, carbonyl functionality, or $\text{Cu}(\text{OH})_2$) [50,51], and (533.3 eV that can be attributed to various C oxide species) [50]. In conclusion, the XPS results confirmed the inclusion of Cu(I/II) species within the pores of

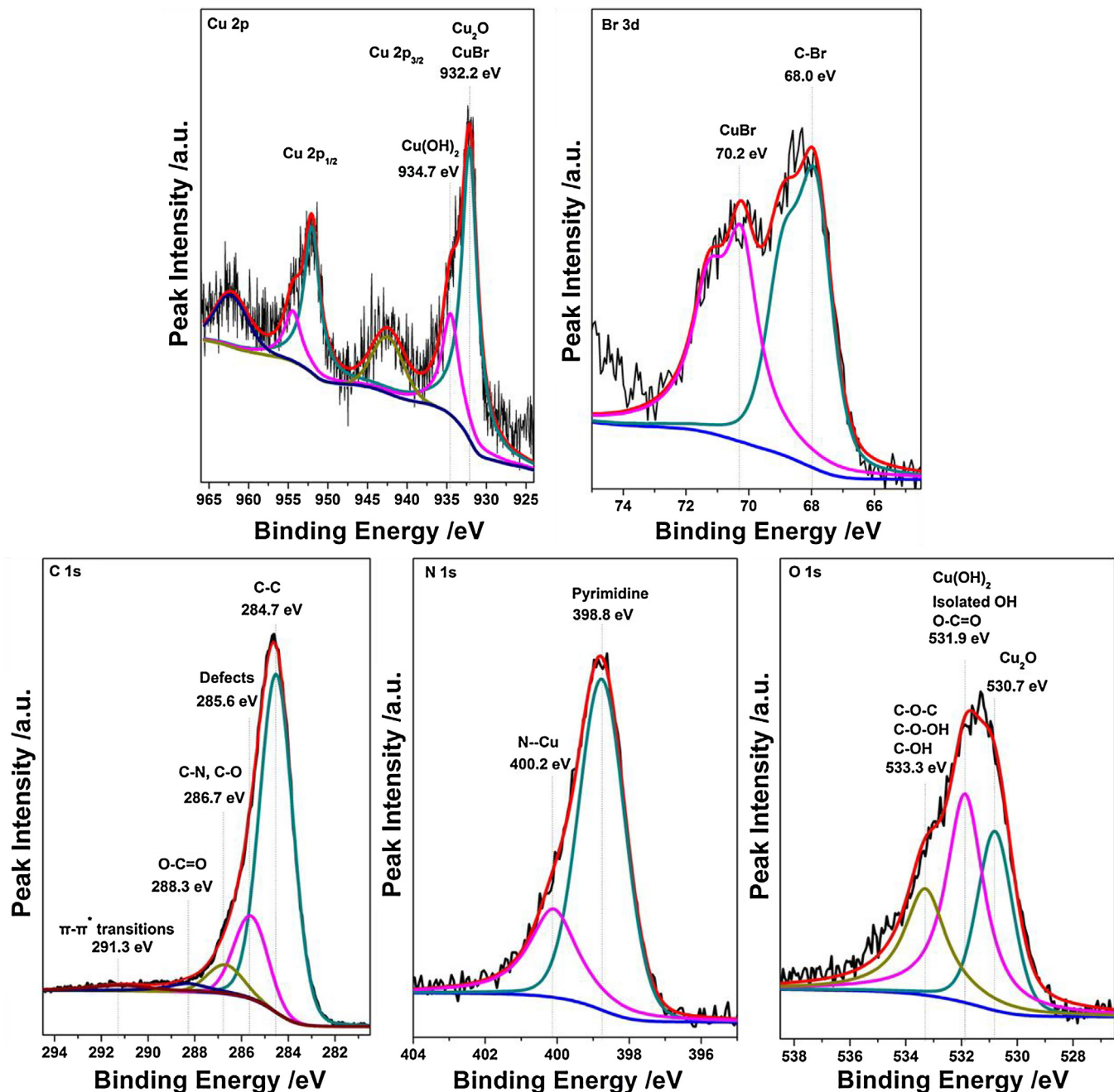


Fig. 11. XPS spectra for the POP-Cu@MWCNTs (labeled spectra).

the POP-Cu@MWCNTs, where CuBr_x ($x = 1, 2$) were simultaneously detected within the sample, potentially due to *in situ* oxidation of the CuBr used in the preparation of the sample.

When compared to several recent reports, the catalytic CO_2 electroreduction activity of our POP@MWCNT composite (onset of -1.22 V vs. Ag|AgCl and a current density of 1.9 mA/cm 2 at -1.6 V) appears below that reported for a Co-porphyrin-based covalent-organic framework (COF) which demonstrated an onset potential of -420 mV RHE @pH 7.2, calculated to be -1.02 V vs. Ag|AgCl @ pH 6.73 of our solution [52]. However, it is worth mentioning the lower cost of our metal-free catalyst as compared to this particular system. Furthermore, the Cu-impregnated version reported here demonstrated comparable activity (when compared to a recently published Cu foam catalyst (3.9 mA/cm 2 for the POP-Cu@MWCNT as compared to ~ 5 mA/cm 2 for the Cu foam catalyst at -1.6 V vs. Ag|

AgCl) [53]. Further investigation is underway to elucidate the effect of different metal ions on the composite catalytic activity towards CO_2 conversion, as well as the mechanistic pathway(s) associated with such processes.

3. Conclusion

Our findings clearly demonstrate that synergy between the POP and the MWCNT has occurred at the molecular level. We find that, when the POP was constructed *in situ* from its soluble MBBs around the MWCNT, desirable properties have spontaneously emerged as a direct result of mixing the chemical functionality of both materials in truly composite structures. Among these properties are the structural rigidity, tunable gas sorption, and activity towards CO_2 electrochemical conversion. Remarkably the synthesis is carried

out in a straightforward, one-pot approach, utilizing unmodified MWCNTs and MBBs of the targeted POP, under mild reaction conditions. This approach enabled the construction of microporous material of appreciable surface area, structural rigidity, CO₂ sorption characteristics, and electrochemical activity, not demonstrated fully in either of its two components separately. This bottom-up approach paves the road for further investigations of relevant systems towards truly heterogeneous electrocatalytic systems benefitting from structural and chemical properties of two different classes of materials, in particular towards CO₂ capture and sequestration, as well as potentially towards sensing applications.

4. Experimental

All reagents were used as received without further purification. Solvents, catalysts, and common chemicals were purchased from Sigma-Aldrich or Fisher Scientific-UK. Brominated aromatics were purchased from Combi-Blocks. Triethynylbenzene was synthesized as described elsewhere [40]. Nitrogen and CO₂ gases for sorption were purchased from Airliquide (N₂ AlphaGaz2 (99.999%) and CO₂ (99.995%)). Carbon Nanotubes (Alfa Aesar Fullerene, nanotube, multi-walled, 20 nm OD, 5–20 μm long 50 mg, Stock #: 43839, Lot #: J30L17) were used as received without further purification. Carbon paste was provided by Bio-Logic Life instruments Cat. No.: 001010, CPO carbon paste oil base 1 g, distributed by BAS Inc.

Gas sorption analysis was performed on Micromeritics ASAP2020 and the variable temperature CO₂ isotherms were recorded in insulated Dewar flask connected to LAUDA RA-8 circulating chiller. The apparent surface areas were determined from the nitrogen adsorption isotherms collected at 77 K by applying the Brunauer-Emmett-Teller (BET) and Langmuir models. Pore size analyses were performed using a slit NLDFT pore model system by assuming a carbon finite pores surface. The determination of the isosteric heats of adsorption (Q_{st}) for CO₂ was estimated by applying the Clausius-Clapeyron expression using the sorption isotherms measured at variable temperatures.

CHN elemental analyses were conducted on ThermoScientific Flash 2000. **Infra-red absorption spectra** were recorded on ThermoScientific Nicolet is-10. **Thermogravimetric analyses** were conducted on Thermal Analysis-Q50. **TEM images** were acquired on a JEOL JEM-2100, operating at 200 KV.

4.1. Computational methods

A possible fragment (oligomer) of the POP containing the aromatic pyrimidine and the triethynylbenzene rings was constructed and then its geometry was optimized with density functional theory (DFT). The B3LYP density function was applied with the 3-21G basis sets in Gaussian 09 [54]. The choice for this basis set was made as it is sufficient for geometry optimization while avoiding unnecessary expensive calculations especially as no electronic structure characteristics of the system are further investigated. For the geometry optimization of the composite, the calculations were initiated from the geometrically optimized oligomer structure placed in proximity of short-length CNT containing 440 atoms, and the geometry optimization calculations re-initiated with the same level of theory.

4.2. XPS measurements

X-ray photoelectron spectroscopy measurements were performed using a Kratos AXIS Ultra DLD XPS system with a monochromatic Al Ka source operated at 15 keV and 150W and a hemispherical energy analyzer. The X-rays were incident at an angle of 45° with respect to the surface normal. Samples were placed in small powder pockets on the holder and analysis was

performed at a pressure below 1 × 10⁻⁹ mbar. High resolution core level spectra were measured with a pass energy of 40 eV. The XPS experiments were performed while using an electron gun directed on the sample, for charge neutralization.

4.3. Synthesis of POP@MWCNTs

In a 100 mL pressure vessel, a mixture of DMF (15 mL) and Et₃N (2 mL) was added, cooled in liquid nitrogen bath, degassed through three freeze-pump-thaw cycles and maintained under nitrogen atmosphere. To this prepared solution was added multi walled carbon nanotubes (8 mg), 4,6-dibromopyrimidine (23 mg, 0.1 mmol), 1,3,5-triethynylbenzene (15 mg, 0.1 mmol), CuI (5 mg, 0.026 mmol), PPh₃ (5 mg, 0.019 mmol) and PdCl₂(PPh₃)₂ (5 mg, 0.014 mmol) and the tube was sonicated for 2 min, then sealed with a Teflon screw under flow of nitrogen. The reaction mixture was then placed in an oil bath maintained at 80 °C for 24 h. A dark green solid was formed which was filtered under vacuum through a sintered glass funnel, washed with DMF, ACN and left to exchange in ACN at 110 °C in sealed vial under autogenous pressure for 1 h, then left at room temperature overnight, filtered under vacuum and left to dry at 110 °C for a few minutes before conducting further analyses. The total dry weight of the solid was 28 mg, 93% yield based on the sum of the masses for starting material excluding the mass of Br atoms.

4.4. Synthesis of POP

For the synthesis of the POP identical synthesis as to the one mentioned above was utilized with the exception of adding the MWCNTs.

4.5. Cu impregnation into the POP@MWCNT

In a 25 mL scintillation vial a 10 mL of 10 mM solution of CuBr was prepared in acetonitrile, to which was added 20 mg of dried POP@MWCNT composite, the vial sealed and left at room temperature for 24 h. The UV-vis spectra were recorded for the impregnation solution before addition of the POP@MWCNT then after the incubation for 24 h. A near complete uptake of the CuBr was evident from the UV-vis spectrum of the supernatant solution. The sample was then washed thoroughly with acetonitrile several times, then incubated in acetonitrile at 80 °C under autogenous pressure in a sealed vial for 2 h, prior to filtration and washing with ACN, then dried at 80 °C oven for 2 h before analysis.

4.6. Electrochemical measurements

In a typical run, 5 mg of the studied solid (POP@MWCNT or POP-Cu@MWCNT) was mixed with 15 mg of carbon paste (Bio-Logic life instruments) and grinded in agate mortar to ensure homogeneous distribution inside the carbon paste. This prepared material was then packed inside a carbon paste electrode (CPE) of 3 mm cross section. The electrochemical measurements were conducted on a biologic SP-50 potentiostat/galvanostat in a three electrodes configuration. The working electrode was a CPE packed with the prepared slurry, Pt wire as a counter electrode and Ag|AgCl (3.5 M KCl) as a reference electrode. The electrolyte was aqueous KHCO₃ (0.1 M) degassed through bubbling of N₂ for 30 min (99.9999%, alphagaz2, Airliquide), or saturated with CO₂ (99.995%, Airliquide), through bubbling for 30 min prior to measurements, the CO₂ flow was also maintained above the solution to ensure maintained CO₂ environment. CO₂ electrocatalytic reduction response was investigated through the linear sweep voltammetry (LSV) technique. The working electrode potential was swept between 0 V to -1 V or up to -2 V with scan rate of 10 mV/s for the LSVs

and 100 mV/s for the CVs in 0.1 M KHCO₃ as the supporting electrolyte.

4.7. AFM imaging

A few fragments of POP@MWCNT were briefly sonicated in isopropanol before being casted on mica and HOPG for AFM measurements. After drying in air, the topographic tapping mode images of the composite were obtained using Bruker Dimension 5000 scanning probe microscope. Good quality images show the structure of the composite where MWCNT ropes are entirely covered by the polymer. It is worth noting that the polymer is entirely rapping every individual MWCNT within the rope as clearly shown at the edge of the rope. Unlike the case of pristine MWCNT, low power sonication of 25 w causes rope to exfoliate easily into individual MWCNT. The images presented here have not processed in anyway.

Author contributions

M.H.A conceived the idea and designed the project. R.R.H and M.H.A carried out the synthesis and most of the characterization, A.H. conducted the AFM measurements, A.B.S designed and conducted the electrochemical experiments and interpreted the results, S.G.K conducted and interpreted the XPS measurements, A.E conducted the TEM analyses. M.A. conducted the quantum mechanical calculations, Y.S.H. conducted the elemental analysis. M.H.A, M.R.B, I.H.H and A.H analyzed the results and co-wrote the manuscript.

Acknowledgements

We acknowledge the funds from Zewail City of Science and Technology-center for materials science, functional materials group, and Egyptian Science and Technology Development Fund (STDF-Grant 6125).

Appendix A. Supplementary data

Supplementary data associated with this article can be found, in the online version, at <http://dx.doi.org/10.1016/j.apcatb.2017.02.009>.

References

- [1] Z.-Z. Yang, L.-N. He, J. Gao, A.-H. Liu, B. Yu, Carbon dioxide utilization with CN bond formation: carbon dioxide capture and subsequent conversion, *Energy Environ. Sci.* 5 (5) (2012) 6602–6639.
- [2] S.H. Kim, K.H. Kim, S.H. Hong, Carbon dioxide capture and use: organic synthesis using carbon dioxide from exhaust gas, *Angew. Chem. Int. Ed.* 53 (3) (2014) 771–774.
- [3] N.S. Lewis, D.G. Nocera, Powering the planet: chemical challenges in solar energy utilization, *Proc. Natl. Acad. Sci.* 103 (43) (2006) 15729–15735.
- [4] M. Eddaoudi, J. Kim, N. Rosi, D. Vodak, J. Wachter, M. O'Keeffe, O.M. Yaghi, Systematic design of pore size and functionality in isoreticular mofs and their application in methane storage, *Science* 295 (5554) (2002) 469–472.
- [5] S. Kitagawa, R. Kitaura, S. i. Noro, Functional porous coordination polymers, *Angew. Chem. Int. Ed.* 43 (18) (2004) 2334–2375.
- [6] A.P. Cote, A.I. Benin, N.W. Ockwig, M. O'Keeffe, A.J. Matzger, O.M. Yaghi, Porous, crystalline, covalent organic frameworks, *Science* 310 (5751) (2005) 1166–1170.
- [7] G. Férey, C. Mellot-Draznieks, C. Serre, F. Millange, Crystallized frameworks with giant pores: are there limits to the possible? *Acc. Chem. Res.* 38 (4) (2005) 217–225.
- [8] H.M. El-Kaderi, J.R. Hunt, J.L. Mendoza-Cortés, A.P. Côté, R.E. Taylor, M. O'Keeffe, O.M. Yaghi, Designed synthesis of 3d covalent organic frameworks, *Science* 316 (5822) (2007) 268–272.
- [9] J.X. Jiang, F. Su, A. Trewin, C.D. Wood, N.L. Campbell, H. Niu, C. Dickinson, A.Y. Ganin, M.J. Rosseinsky, Y.Z. Khimyak, Conjugated microporous poly(Aryleneethynylene) networks, *Angew. Chem. Int. Ed.* 46 (45) (2007) 8574–8578.
- [10] M.H. Alkordi, Y. Liu, R.W. Larsen, J.F. Eubank, M. Eddaoudi, Zeolite-Like metal-organic frameworks as platforms for applications: on metallocporphyrin-based catalysts, *J. Am. Chem. Soc.* 130 (38) (2008) 12639–12641.
- [11] P. Kaur, J.T. Hupp, S.T. Nguyen, Porous organic polymers in catalysis: opportunities and challenges, *ACS Catal.* 1 (7) (2011) 819–835.
- [12] I. Omae, Recent developments in carbon dioxide utilization for the production of organic chemicals, *Coord. Chem. Rev.* 256 (13–14) (2012) 1384–1405.
- [13] M. Cokoja, C. Bruckmeier, B. Rieger, W.A. Herrmann, F.E. Kühn, Transformation of carbon dioxide with homogeneous transition-metal catalysts: a molecular solution to a global challenge? *Angew. Chem. Int. Ed.* 50 (37) (2011) 8510–8537.
- [14] J. Mao, L. Yang, P. Yu, X. Wei, L. Mao, Electrocatalytic four-electron reduction of oxygen with copper (II)-based metal-organic frameworks, *Electrochim. Commun.* 19 (2012) 29–31.
- [15] H. Wang, F. Yin, B. Chen, G. Li, Synthesis of an²-MnO₂/metal-organic-framework composite and its electrocatalysis towards oxygen reduction reaction in an alkaline electrolyte, *J. Mater. Chem. A* 3 (31) (2015) 16168–16176.
- [16] M. Jiang, L. Li, D. Zhu, H. Zhang, X. Zhao, Oxygen reduction in the nanocage of metal-organic frameworks with an electron transfer mediator, *J. Mater. Chem. A* 2 (15) (2014) 5323–5329.
- [17] M. Jahan, Z. Liu, K.P. Loh, A graphene oxide and copper-centered metal organic framework composite as a tri-Functional catalyst for her, oer, and orr, *Adv. Funct. Mater.* 23 (43) (2013) 5363–5372.
- [18] Q. Bao, Electrocatalytically active graphene-porphyrin mof composite for oxygen reduction reaction, *J. Am. Chem. Soc.* 134 (15) (2012) 6707–6713.
- [19] H. Barkholtz, L. Chong, Z. Kaiser, T. Xu, D.-J. Liu, Highly active non-Pgm catalysts prepared from metal organic frameworks, *Catalysts* 5 (2) (2015) 955.
- [20] L. Sun, M.G. Campbell, M. Dincă, Electrically conductive porous metal-organic frameworks, *Angew. Chem. Int. Ed.* 55 (11) (2016) 3566–3579.
- [21] E.M. Miner, T. Fukushima, D. Sheberla, L. Sun, Y. Surendranath, M. Dinca, Electrochemical oxygen reduction catalysed by Ni₃(Hexaiminotriphenylene)2, *Nat. Commun.* 7 (2016).
- [22] M.G. Campbell, S.F. Liu, T.M. Swager, M. Dincă, Chemiresistive sensor arrays from conductive 2d metal-organic frameworks, *J. Am. Chem. Soc.* 137 (43) (2015) 13780–13783.
- [23] S. Duhović, M. Dincă, Synthesis and electrical properties of covalent organic frameworks with heavy chalcogens, *Chem. Mater.* 27 (16) (2015) 5487–5490.
- [24] C. Lu, T. Ben, S. Xu, S. Qiu, Electrochemical synthesis of a microporous conductive polymer based on a metal-organic framework thin film, *Angew. Chem. Int. Ed.* 53 (25) (2014) 6454–6458.
- [25] P. Wang, Q. Wu, L. Han, S. Wang, S. Fang, Z. Zhang, S. Sun, Synthesis of conjugated covalent organic frameworks/graphene composite for supercapacitor electrodes, *RSC Adv.* 5 (35) (2015) 27290–27294.
- [26] M. Calik, F. Auras, L.M. Salonen, K. Bader, I. Grill, M. Handloser, D.D. Medina, M. Dogru, F. Löbermann, D. Trauner, A. Hartschuh, T. Bein, Extraction of photogenerated electrons and holes from a covalent organic framework integrated heterojunction, *J. Am. Chem. Soc.* 136 (51) (2014) 17802–17807.
- [27] F. Xu, S. Jin, H. Zhong, D. Wu, X. Yang, X. Chen, H. Wei, R. Fu, D. Jiang, Electrochemically active, crystalline, mesoporous covalent organic frameworks on carbon nanotubes for synergistic lithium-ion battery energy storage, *Sci. Rep.* 5 (2015) 8225.
- [28] Q. Liu, Z. Tang, M. Wu, Z. Zhou, Design, preparation and application of conjugated microporous polymers, *Polym. Int.* 63 (3) (2014) 381–392.
- [29] X. Zou, H. Ren, G. Zhu, Topology-directed design of porous organic frameworks and their advanced applications, *Chem. Commun.* 49 (38) (2013) 3925–3936.
- [30] M.H. Alkordi, L.J. Weselinski, V. D'Elia, S. Barman, A. Cadiua, M.N. Hedhili, A.J. Cairns, R.G. AbdulHalim, J.-M. Basset, M. Eddaoudi, Co₂ conversion: the potential of porous-organic polymers (Pops) for catalytic co₂-epoxide insertion, *J. Mater. Chem. A* 4 (19) (2016) 7453–7460.
- [31] M.H. Alkordi, R.R. Haikal, Y.S. Hassan, A.-H. Emwas, Y. Belmabkhout, Poly-functional porous-organic polymers to access functionality – co₂ sorption energetic relationships, *J. Mater. Chem. A* 3 (45) (2015) 22584–22590.
- [32] Y. Xu, S. Jin, H. Xu, A. Nagai, D. Jiang, Conjugated microporous polymers: design, synthesis and application, *Chem. Soc. Rev.* 42 (20) (2013) 8012–8031.
- [33] R. Dawson, A.I. Cooper, D.J. Adams, Nanoporous organic polymer networks, *Prog. Polym. Sci.* 37 (4) (2012) 530–563.
- [34] S. Iijima, Helical microtubules of graphitic carbon, *Nature* 354 (6348) (1991) 56–58.
- [35] J.W. Mintmire, B.J. Dunlap, C.T. White, Are fullerene tubules metallic? *Phys. Rev. Lett.* 68 (5) (1992) 631–634.
- [36] P.J.F. Harris, *Carbon Nanotubes and Related Structures*, Cambridge University Press, 1999.
- [37] C. Jianwei, Ç. Tahir, A.G. William III, Thermal conductivity of carbon nanotubes, *Nanotechnology* 11 (2) (2000) 65.
- [38] C.D. Wood, B. Tan, A. Trewin, F. Su, M.J. Rosseinsky, D. Bradshaw, Y. Sun, L. Zhou, A.I. Cooper, Microporous organic polymers for methane storage, *Adv. Mater.* 20 (10) (2008) 1916–1921.
- [39] V. Guillerm, L.J. Weselinski, M. Alkordi, M.I.H. Mohideen, Y. Belmabkhout, A.J. Cairns, M. Eddaoudi, Porous organic polymers with anchored aldehydes: a new platform for post-synthetic amine functionalization en route for enhanced co₂ adsorption properties, *Chem. Commun.* 50 (16) (2014) 1937–1940.

[40] A.B. Soliman, R.R. Haikal, Y.S. Hassan, M.H. Alkordi, The potential of a graphene-supported porous-organic polymer (Pop) for co₂ electrocatalytic reduction, *Chem. Commun.* 52 (81) (2016) 12032–12035.

[41] A.K. Sekizkardes, T. İslamoğlu, Z. Kahveci, H.M. El-Kaderi, Application of pyrene-derived benzimidazole-linked polymers to Co₂ separation under pressure and vacuum swing adsorption settings, *J. Mater. Chem. A* 2 (31) (2014) 12492–12500.

[42] O.A. Baturina, Q. Lu, M.A. Padilla, L. Xin, W. Li, A. Serov, K. Artyushkova, P. Atanassov, F. Xu, A. Epshteyn, T. Brintlinger, M. Schuette, G.E. Collins, Co₂ electroreduction to hydrocarbons on carbon-supported Cu nanoparticles, *ACS Catal.* 4 (10) (2014) 3682–3695.

[43] W. Tang, A.A. Peterson, A.S. Varela, Z.P. Jovanov, L. Bech, W.J. Durand, S. Dahl, J.K. Norskov, I. Chorkendorff, The importance of surface morphology in controlling the selectivity of polycrystalline copper for co₂ electroreduction, *Phys. Chem. Chem. Phys.* 14 (1) (2012) 76–81.

[44] S. González, M. Pérez, M. Barrera, A.R. González Elipe, R.M. Souto, Mechanism of copper passivation in aqueous sodium carbonate-bicarbonate solution derived from combined X-Ray photoelectron spectroscopic and electrochemical data, *J. Phys. Chem. B* 102 (28) (1998) 5483–5489.

[45] M. Pérez Sánchez, M. Barrera, S. González, R.M. Souto, R.C. Salvarezza, A.J. Arvia, Electrochemical behaviour of copper in aqueous moderate alkaline media, containing sodium carbonate and bicarbonate, and sodium perchlorate, *Electrochim. Acta* 35 (9) (1990) 1337–1343.

[46] S. Fang, X. Dong, Y. Zhang, M. Kang, S. Liu, F. Yan, L. He, X. Feng, P. Wang, Z. Zhang, One-step synthesis of porous cuprous oxide microspheres on reduced graphene oxide for selective detection of mercury ions, *New J. Chem.* 38 (12) (2014) 5935–5942.

[47] S.-G. Liu, P.-J. Wu, X.-Y. Yang, D.-B. Zhu, Four new et- and ttm-Ttf-based ct salts with Cu-containing binuclear polyhalide complex anions: synthesis, properties, and structure, *Mole. Cryst. Liq. Cryst. Sci. Technol. A* 269 (1) (1995) 133–147.

[48] M. Chen, J. Xiao, H.-P. Steinrück, S. Wang, W. Wang, N. Lin, W. Hieringer, J.M. Gottfried, Combined photoemission and scanning tunneling microscopy study of the surface-assisted ullmann coupling reaction, *J. Phys. Chem. C* 118 (13) (2014) 6820–6830.

[49] R.P. Vasquez, Cubr by Xps, *Surf. Sci. Spectra* 2 (2) (1993) 144–148.

[50] V. Datsyuk, M. Kalyva, K. Papagelis, J. Parthenios, D. Tasis, A. Siokou, I. Kallitsis, C. Gallois, Chemical oxidation of multiwalled carbon nanotubes, *Carbon* 46 (6) (2008) 833–840.

[51] N.S. McIntyre, S. Sunder, D.W. Shoesmith, F.W. Stanchell, Chemical information from Xps—applications to the analysis of electrode surfaces, *J. Vacuum Sci. Technol.* 18 (3) (1981) 714–721.

[52] Y. Ye, L. Zhang, Q. Peng, G.-E. Wang, Y. Shen, Z. Li, L. Wang, X. Ma, Q.-H. Chen, Z. Zhang, S. Xiang, High anhydrous proton conductivity of imidazole-Loaded mesoporous polyimides over a wide range from subzero to moderate temperature, *J. Am. Chem. Soc.* 137 (2) (2015) 913–918.

[53] S. Sen, D. Liu, G.T.R. Palmore, Electrochemical reduction of co₂ at copper nanofoams, *ACS Catal.* 4 (9) (2014) 3091–3095.

[54] M.J. Frisch, G.W. Trucks, H.B. Schlegel, G.E. Scuseria, M.A. Robb, J.R. Cheeseman, G. Scalmani, V. Barone, B. Mennucci, G.A. Petersson, H. Nakatsuji, M. Caricato, X. Li, H.P. Hratchian, A.F. Izmaylov, J. Bloino, G. Zheng, J.L. Sonnenberg, M. Hada, M. Ehara, K. Toyota, R. Fukuda, J. Hasegawa, M. Ishida, T. Nakajima, Y. Honda, O. Kitao, H. Nakai, T. Vreven, J.A. Montgomery Jr., J.E. Peralta, F. Ogliaro, M.J. Bearpark, J. Heyd, E.N. Brothers, K.N. Kudin, V.N. Staroverov, R. Kobayashi, J. Normand, K. Raghuvaran, A.P. Rendell, J.C. Burant, S.S. Iyengar, J. Tomasi, M. Cossi, N. Rega, N.J. Millam, M. Klene, J.E. Knox, J.B. Cross, V. Bakken, C. Adamo, J. Jaramillo, R. Comberts, R.E. Stratmann, O. Yazyev, A.J. Austin, R. Cammi, C. Pomelli, J.W. Ochterski, R.L. Martin, K. Morokuma, V.G. Zakrzewski, G.A. Voth, P. Salvador, J.J. Dannenberg, S. Dapprich, A.D. Daniels, Ö. Farkas, J.B. Foresman, J.V. Ortiz, J. Cioslowski, D.J. Fox, *Gaussian 09*, Gaussian, Inc., Wallingford, CT, USA, 2009.